RSC Advances

REVIEW

View Article Online
View Journal | View Issue

Cite this: *RSC Adv.*, 2020, **10**, 29408

Recent advancements in g-C_3N_4-based photocatalysts for photocatalytic CO_2 reduction: a mini review

Runlu Liu,[a] Zhixin Chen,[b] Yao Yao,[a] Yao Li,*[a] Waqas A. Cheema,[c] Dawei Wang[d] and Shenmin Zhu*[a]

Carbon dioxide (CO_2) is a very important micro-molecular resource. Using CO_2 captured from the atmosphere for high-output synthesis of chemicals as raw materials has great significance and potential for various industrial applications. Since the industrial revolution in the 18th century, manmade CO_2 emission has increased by 45%, which negatively impacts the planetary climate by the so-called greenhouse effect. Therefore, high-efficiency photocatalysis and photocatalysts for CO_2 conversion have become the most important challenges and milestones throughout the world. In consideration of this, various catalysts have been explored. Among these, graphitic carbon nitride (g-C_3N_4) as a semiconductor is emerging as a highly promising photocatalyst for removing CO_2 from the atmosphere. Moreover, due to its excellent chemical stability and unique band structure, g-C_3N_4 has exhibited significant application potential for photocatalysis. This review summarizes the advancements that have been made in the synthesis and photocatalytic applications of g-C_3N_4-based catalysts for CO_2 reduction in recent years and explains the future challenges and prospects in this vital area of research.

Received 2nd July 2020
Accepted 27th July 2020

DOI: 10.1039/d0ra05779g

rsc.li/rsc-advances

1. Introduction

Carbon dioxide (CO_2) is a major greenhouse gas that contributes approximately 20% to the greenhouse effect. Its emissions are increasing and are causing a significant negative influence on the overall climate and life on our planet. It was reported that the annual global carbon dioxide emissions have exceeded 30 billion tons, and only 1% of this amount is being removed annually.[1] However, these emissions are not considered to be solely waste because CO_2 is a very important micro-molecular resource for many industrial chemicals, such as methane, methyl alcohol, and dimethylformamide (DMF). Artificial synthesis of industrial-scale chemicals with CO_2 captured from the atmosphere not only removes the harmful CO_2, but also produces valuable chemical products for industries.

[a]State Key Laboratory of Metal Matrix Composites, Shanghai Jiao Tong University, Shanghai 200240, China. E-mail: smzhu@sjtu.edu.cn
[b]School of Mechanical, Materials, Mechatronics and Biomedical Engineering, University of Wollongong, Wollongong, 2522, Australia
[c]Industrial Technology Development Center (ITDC), Higher Education Intelligence (HEI) Project, Pakistan
[d]School of Chemical Engineering, UNSW Australia, Sydney, NSW 2052, Australia

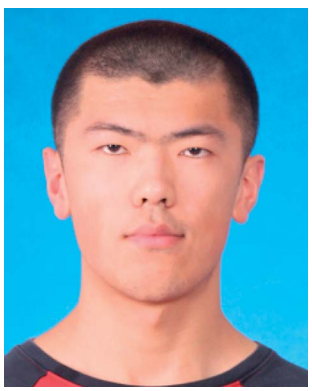

Mr Runlu Liu received his Bachelor degree in Materials Science and Engineering from Shanghai Jiao Tong University, China in 2019. He is presently a postgraduate student at the School of Materials Science and Engineering in Shanghai Jiao Tong University, under the supervision of Prof. Shenmin Zhu. He is currently working on the research of g-C_3N_4-based nanocomposites and their applications in photocatalysis.

Dr Yao Li received his PhD in Material Science from Shanghai Jiao Tong University, China in 2015 under the supervision of Prof. Di Zhang and Prof. Shenmin Zhu. He joined as a research associate at Shanghai Jiao Tong University at 2015. He is working on the research of bio-inspired material and carbon matrix material, as well as their application in environmental treatment and energy storage.

Since 1970, it has been a challenge worldwide to develop a facile and efficient method for the photocatalytic reduction of CO_2. Three types of CO_2 photoreduction systems have been developed, *i.e.*, the semiconductor photocatalytic system, the metal complex photocatalytic system, and the enzyme photocatalytic system.[2] In 1979, Fujishima *et al.* reported photocatalytic CO_2 reduction using semiconductors TiO_2 and CdS as photocatalysts, and these were among the earliest photocatalytic systems for CO_2 reduction.[3] In 1983, Lehn *et al.* reported for the first time a CO_2 reduction system using *fac*-$Re(bpy)(CO)_3Cl$ as a photocatalyst, and it exhibited high selectivity and high quantum yield.[4] In 1986, Willner *et al.* reported a photocatalytic CO_2 reduction system using enzymes as catalysts.[5]

Since their discoveries, all three types of CO_2 photoreduction systems have been significantly developed. Due to the high substrate specificity, high conversion rates, excessive sensitivity, high cost, and narrow applicability of the enzymatic catalysts, their broad utilization has been limited.[6] Thus, most of the interest has been focused on semiconductor or metal complex-based catalysts. In general, metal complex systems are based on homogeneous organic photocatalysts. Because all the metal atoms can serve as active sites, the catalytic efficiency and selectivity of the metal complex systems are sensitive to energy distribution. Moreover, due to the homogeneous structure, there are few side reactions accompanying metal complex photocatalysis.[7,8] However, it is difficult to separate reactants from products because of the homogeneous structure, which limits the cyclic utilization and can be disadvantageous for sustainable development. In comparison, semiconductor-based photocatalysts are mostly heterogeneous catalysts, and with their use, it is easier to separate products from the reaction system.[9] Furthermore, the photocatalytic performance can be improved through various structural and chemical modifications of the photocatalyst, *e.g.*, porous semiconductor photocatalysts, doping[10–14] or compositing of a semiconductor photocatalyst with other materials.[15–17] Thus, there has been great interest and widespread usage of semiconductor photocatalysis during recent years.

Among the various types of semiconductors, graphitic carbon nitride (g-C_3N_4) is considered promising because it is composed of triazine rings and tri-*s*-triazine (heptazine) rings as its basic unit, and it forms a two-dimensional lamellar structure (Fig. 1).[18] Because of the structure, it is insoluble in most solvents such as water, ethanol, ether, toluene, DMF, and tetrahydrofuran (THF).[19] g-C_3N_4 is a typical polymer semiconductor with a band gap of 2.7 eV that can absorb blue-violet light with a wavelength less than 475 nm in the solar spectrum,[20] and thus, it is a potential candidate for photocatalysis.[21,22] In 2009, Wang *et al.* for the first time reported photocatalytic hydrogen production using g-C_3N_4 as a photocatalyst.[23] In 2013, Peng *et al.* used g-C_3N_4 in CO_2 photoreduction.[24] This review will focus on the present pathways for the applications of g-C_3N_4 in the field of photocatalytic CO_2 reduction. Finally, the conclusion of the article addresses the current challenges and future development of g-C_3N_4-based photocatalysts.

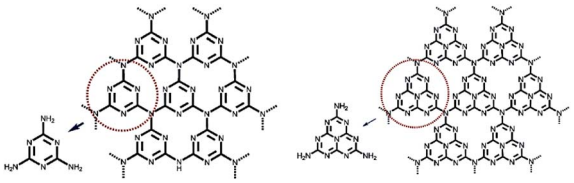

Fig. 1 *s*-Triazine (left) and tri-*s*-triazine (right) as tectons of g-C_3N_4.[18] Copyright 2012 WILEY-VCH.

2. Fundamentals of photocatalytic CO_2 reduction on semiconductors

Photocatalytic CO_2 reduction is a process where light energy is used as the input energy, and the product can be controlled by changing the reaction conditions and types of catalysts.[25,26] The common reaction pathways are listed as follows.

$$CO_2 + 2H^+ + 2e^- \rightarrow HCOOH,\ E^0 = -0.61\ V \quad (I)$$

$$CO_2 + 2H^+ + 2e^- \rightarrow CO + H_2O,\ E^0 = -0.53\ V \quad (II)$$

$$CO_2 + 4H^+ + 4e^- \rightarrow HCHO + H_2O,\ E^0 = -0.48\ V \quad (III)$$

$$CO_2 + 6H^+ + 6e^- \rightarrow CH_3OH + H_2O,\ E^0 = -0.38\ V \quad (IV)$$

$$CO_2 + 8H^+ + 8e^- \rightarrow CH_4 + 2H_2O,\ E^0 = -0.24\ V \quad (V)$$

The principle of photocatalytic CO_2 reduction consists of five main steps: light adsorption (i), charge separation (ii), CO_2 adsorption (iii), surface redox reaction (iv), and product desorption (v).[27] To trigger the CO_2 reduction reaction, the conduction band edge of the photocatalysts should be more negative than the reaction potential, and they are listed above (*vs.* NHE).[28] To achieve efficient generation and transfer of photo-excited electrons and holes, certain modifications of photocatalysts are required. To increase the effectiveness of the process, a semiconductor-based photocatalyst should be designed considering these issues.

First, a semiconductor with a band gap of 2.0–3.0 eV is ideal for visible light adsorption.[27] Second, the separation of

Prof. Shenmin Zhu received her PhD degree from Shanghai Jiao Tong University in 2001. She is presently a professor at the School of Materials Science and Engineering, State Key Lab of Metal Matrix Composites, Shanghai Jiao Tong University. Her current fields of interest are graphene-based functional materials, porous carbon, and bio-inspired photonic crystals with stimuli-responsive properties.

electron–hole pairs is sufficiently large so that the recombination of electrons and holes is limited.[30] Third, to enhance the adsorption of CO_2, the surface area of photocatalysts should be enlarged, which can be accomplished by providing more active sites or introducing alkaline components into the photocatalysts.[31] Fourth, to improve the efficiency of surface redox reactions, one can introduce a cocatalyst or prepare composites to enhance the charge transfer rate. Finally, accurate timing of the release of the products is necessary to increase the conversion and reaction rate.

3. g-C_3N_4 as photocatalyst

A good photocatalyst requires a suitable energy band structure to ensure light harvesting ability and efficient charge transfer. Among varieties of photocatalysts, oxide semiconductors usually have too large band gap energies to sufficiently utilize incident light, while the chalcogenide semiconductors often have a narrow band gap, which results in easy recombination of the photogenerated charge carriers (Fig. 2). In comparison, g-C_3N_4 is a non-metal semiconductor with a band gap of 2.7 eV and suitable conduction band (CB) and valence band (VB) positions, enabling it to absorb visible light. Moreover, g-C_3N_4 can be prepared by facile methods, and the microstructure of g-C_3N_4 can be easily adjusted to create pores as active sites or enlarge the surface area for more optimal light absorption. Because of these advantages, g-C_3N_4 is a superior photocatalyst for visible-light-driven CO_2 reduction compared to TiO_2 and other common photocatalysts. However, because the 2.7 eV band gap of g-C_3N_4 is insufficiently large, the separated electron–hole pairs tend to recombine, thus limiting the effective separation of charges and subsequent redox reactions. Although it has numerous Lewis base sites, *e.g.*, Brønsted base sites and nucleophile sites that are favourable for CO_2 adsorption, bulk g-C_3N_4 prepared by direct calcination has a relatively small surface area. Therefore, several modifications including structural tuning,[31–37] elemental doping,[38–45] addition of cocatalyst,[46–60] and compositing[61–70] have been used to increase the adsorption and obtain more effective charge separation.

3.1 g-C_3N_4 with nanostructures and/or defects

It is expected that g-C_3N_4 has good potential for CO_2 fixation and activation. However, the bulk form obtained from some precursors has a small surface area, and thus, has low adsorption efficiency and catalytic activity. To alleviate this drawback, researchers have taken specific measures to increase the surface area and improve the functionality of g-C_3N_4. In this regard, Zhang *et al.* applied porous structured g-C_3N_4 to a CO_2 photocatalytic reduction to CO under visible light irradiation.[31] Moreover, the g-C_3N_4 was synthesized by calcination, using either melamine or melamine hydrochloride as the precursor. It was found that the latter has a surface area 39 times greater than bulk g-C_3N_4 due to the porous structure, but the performance of CO_2 photoreduction was not obviously improved. This occurred because the porous structure not only endows g-C_3N_4 with a higher surface area but also enlarges the band gap, which resulted in more difficult electron excitation and the lower yield of CO_2. Although it failed to improve the performance of CO_2 photoreduction, there was still direct significance to this pioneering research in that the structural tuning of g-C_3N_4 resulted in great improvement of the photoreactivity.

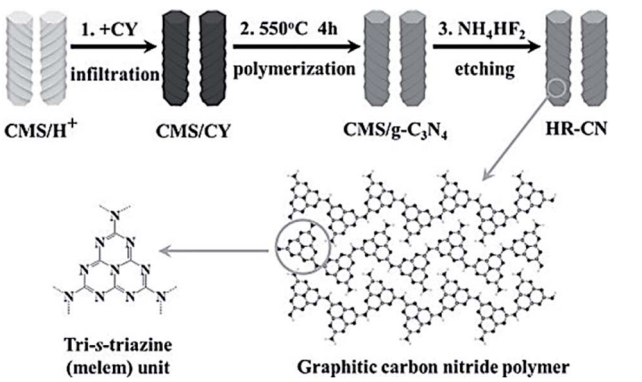

Fig. 3 Synthetic process for helical nanorod-like graphitic carbon nitride (HR-CN) based on chiral mesoporous silica (CMS) as the template and cyanamide (CY) as the precursor.[32] Copyright 2014, Wiley-VCH.

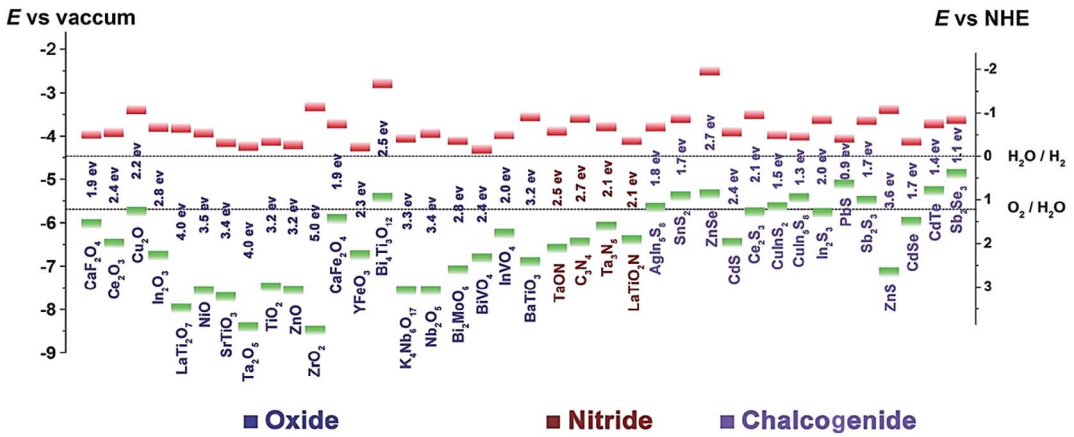

Fig. 2 Band gap energies and CB (green) and VB (red) edge positions of the selected photocatalysts with respect to the vacuum level and NHE. The two dashed lines indicate the water redox reaction potentials.[29] Copyright 2016 WILEY-VCH.

Thus far, different varieties of g-C_3N_4 nanostructures have been developed, such as porous structures, 1D nanorods, nanowires, 2D nanosheets, and 3D nanostructures.[32–37] As a typical example, Zheng and Wang *et al.* imprinted helical g-C_3N_4 nanorods with chiral silicon dioxide as templates (Fig. 3).[32] This helical structure caused multiple reflections of incident light, leading to an improved light-harvesting capability across the entire optical spectrum. Although the band gap increased from 2.66 eV to 2.75 eV, the helical g-C_3N_4 still exhibited an overall enhanced optical absorption compared to bulk g-C_3N_4. A lower photoluminescence (PL) intensity and a stronger PL quenching was measured for the helical g-C_3N_4 nanorods as compared to the bulk g-C_3N_4, which indicated that the recombination of photogenerated charge carriers in the helical g-C_3N_4 nanorods was suppressed.[71] The CO production and selectivity of the helical g-C_3N_4 system during visible-light CO_2 reduction reached 8.9 μmol and 96.7%, respectively. In recent years, there has been much experimentation with 2D g-C_3N_4 nanosheets because of their large specific surface area, which is advantageous for light harvesting and gas adsorption. Cao *et al.* prepared ultra-thin g-C_3N_4 nanosheets through a stepwise NH_3-mediated thermal exfoliation approach.[33] The resulting nanosheets were approximately 3 nm thick and were produced with a hierarchical structure due to the amine-induced assembly. This structure endowed g-C_3N_4 nanosheets with a much higher specific surface area, abundant active sites, shorter diffusion distance of charge carriers, and increased CO_2 adsorption. Therefore, the yields of CH_4 and CH_3OH with g-C_3N_4 nanosheets as catalyst were 9.93 and 5.34 times higher than that with bulk g-C_3N_4 as catalyst, respectively.

Apart from structural tuning, the introduction of defects is also a useful method for promoting the photoactivity of g-C_3N_4. Zhang *et al.* introduced carbon vacancies into synthesized g-C_3N_4 with urea and heat treatment under an NH_3 atmosphere to enhance CO photogeneration.[34] The g-C_3N_4 with enriched C vacancies exhibited a CO evolution rate of 4.18 μmol g^{-1} h^{-1}, which was 2.3 times higher than the evolution rate of pristine g-C_3N_4. The improved CO_2 reduction performance was ascribed to greater CO_2 adsorption and activation, an upshifted conduction band, increased charge carrier concentration, and prolonged lifetime. Furthermore, the reactive oxygen species (ROS) and electrochemical impedance spectroscopy (EIS) indicated that the C vacancies could weaken the exciton effect and elevate the charge carrier generation.

In another study, Chai *et al.* introduced N vacancies into ultrathin g-C_3N_4 nanosheets using NH_4Cl as a dynamic gas template.[35] The NH_4Cl decomposed into NH_3 and HCl gases upon heating, which formed a bubble film on the surface of the polymerized g-C_3N_4 nanosheets. As the π–π interlayer interactions in the g-C_3N_4 nanosheets became diminished with the expansion of the bubble film, an ultrathin bubble g-C_3N_4 film formed, and N vacancies were introduced afterwards by a post-treatment under a reducing atmosphere. The few-atomic-layered structure enlarged the exposed surface area, and this benefited charge carrier transportation. Additionally, N vacancies induced a mid-gap state, which facilitated multi-electron excitation in a two-step process and extended the optical

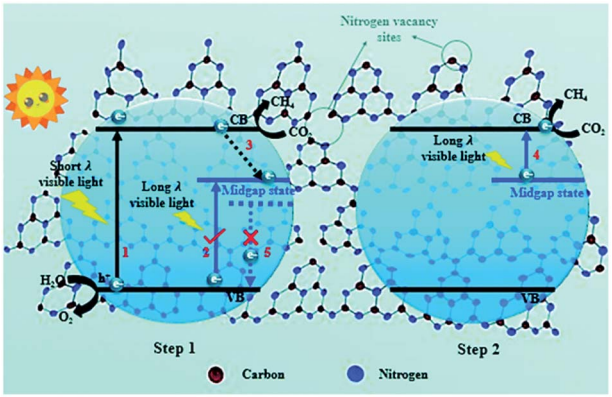

Fig. 4 Schematic illustration of nitrogen defect-modified g-C_3N_4 atomic layers for photocatalytic CH_4 evolution from CO_2.[35] Copyright 2019, Royal Society of Chemistry.

absorption of the g-C_3N_4 nanosheets to the near infrared region, and thus, the utilization of solar energy was enhanced (Fig. 4). Furthermore, N vacancies could also result in an aftereffect where the decay lifetime was prolonged because the mid-gap state retarded the radiative recombination rate. The g-C_3N_4 nanosheets with N vacancies exhibited a 5.14-fold higher CH_4 evolution rate than pristine g-C_3N_4. This pioneering work was intriguing and inspiring because it highlighted the synergistic effect of morphology control and vacancy modulation on photocatalytic CO_2 reduction.

Both structural adjustment and defect tuning are meant to change the energy band structure of g-C_3N_4 to enhance the light-harvesting ability and charge transfer efficiency, and they are the most convenient methods to improve the photocatalytic performance of g-C_3N_4.

3.2 Non-metal doped g-C_3N_4

Pristine g-C_3N_4 exhibits a poor performance due to low CO_2 absorption and poor utilization of photo-excited charge carriers because of the deficiency of electron donation sites and unoptimized electronic structure.[37] To address these challenges, heteroatom doping was developed to tune the electronic structure of g-C_3N_4. The doped elements included mainly B, C, O, P, and S.[38–41]

In g-C_3N_4, N atoms are active sites for photocatalytic reactions, and the electrons are mainly localized around N atoms. Under light irradiation, transfer of excited electrons from N atoms to C atoms is difficult due to the localized electron structure.[72–74] Moreover, the excited electrons are expected to transfer back for redox reaction, which increases the chances of recombination of the charge carriers. To address these problems, Liu *et al.* prepared boron-doped g-C_3N_4 by a one-step calcination using boric acid and urea as precursors.[38] B atoms were doped into cavities between adjacent tri-*s*-triazine units through coordination with N atoms. The density functional theory (DFT) studies demonstrated that doping of B introduced a new electron excitation pathway from N ($2p_x$, $2p_y$) to B ($2p_x$, $2p_y$), which improved the charge transfer and localization, and

thus the reaction dynamics. Furthermore, the doped B atoms altered the gas adsorption on the surface of g-C_3N_4 so that they could subsequently act as active sites. Consequently, the optimal B-doped g-C_3N_4 resulted in a 32-fold higher yield of CH_4 than that of pure g-C_3N_4.

In another work, Tian *et al.* synthesized phosphorus-doped g-C_3N_4 nanotubes by calcinating a mixture of melamine and sodium hypophosphite monohydrate.[39] The nanotube structure attained a much larger surface area than that of g-C_3N_4 nanosheets. The doping of phosphorus resulted in a shifting down of the conduction band and valence band of g-C_3N_4, and the band gap was narrowed by 0.12 eV (Fig. 5), which enhanced the optical absorption. The phosphorus doping also created additional amino groups in the surface of g-C_3N_4, which increased CO_2 adsorption due to the acid–base interaction. As a result, the gas yields were 9.48 μmol g^{-1} for CO and 7.24 μmol g^{-1} for CH_4, which were 3.12 and 13.9 times the yield of pristine g-C_3N_4, respectively. Similarly, Yu *et al.* fabricated sulfur-doped g-C_3N_4 (TCN) by a facile calcinating method using thiourea as the precursor.[40] According to UV-Vis diffuse reflection spectra (UV-Vis DRS), the band gap of TCN was 2.63 eV, which was 0.07 eV narrower than that of un-doped g-C_3N_4 (MCN). This narrow band gap enabled TCN to absorb more solar energy and produce more charge carriers, thus improving the photocatalytic performance. According to the theoretical calculation, however, the band gaps of TCN and MCN were the same, but an impurity level was introduced due to sulfur doping on TCN. The photoelectrons could jump from the VB to the impurity level or from the impurity level to the CB. As a result, the CH_3OH yield of TCN was 2.5 times greater than that of MCN.

It is worth noting that many studies have been recently conducted on metal and non-metal co-doped g-C_3N_4 for CO_2 photoreduction. Metal elements such as K, Na, and Co can improve the photocatalytic performance through a similar mechanism.[42–45] Zheng *et al.* prepared N vacancy-rich g-C_3N_4 co-doped with B and K atoms through a one-step method.[42] In this system, K functioned as an electron donor and promoted interlayer electron transfer, B assisted in maintaining a high reduction potential and counteracted the drawbacks of K, and N vacancies lowered the conduction band minimum (CBM) and promoted CO_2 absorption. The synergistic effect of the multiple modifications significantly improved the CO_2 reduction performance. The CH_4 and CO produced in 5 h were 5.93 μmol g^{-1} and 3.16 μmol g^{-1}, respectively, and 161% and 527% of the production of the pristine g-C_3N_4 occurred under the same conditions. It further suggested that the combination of doping and vacancies enhanced the photocatalytic performance of g-C_3N_4, and provides a new strategy for photocatalyst modification.

Overall, the non-metal doping increased the CO_2 photoreduction activity of g-C_3N_4 by tuning the energy band structure, which manifested as a narrower band gap that provided more effective light absorption in a wider range of spectra, especially in the visible light region. The non-metal doping could also introduce an impurity level or a new electron excitation pathway to g-C_3N_4, which facilitated the charge transfer. Moreover, the doping process might introduce surface groups, which improved CO_2 adsorption due to the acid–base interaction.

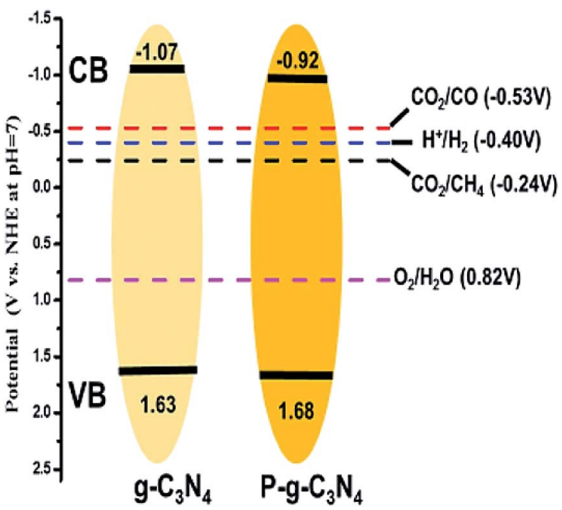

Fig. 5 The electronic structure and all reaction reduction potentials of hydrogen evolution and CO_2 conversion into CO and CH_4.[39] Copyright 2018, American Chemical Society.

3.3 g-C_3N_4 with co-catalyst

In photocatalysis, suitable co-catalysts can serve as active sites for surface reactions and improve charge separation and charge utilization.[75] For a semiconductor such as g-C_3N_4, frequently used co-catalysts include metal, carbon materials, reduction co-catalyst, and double co-catalyst.[76]

3.3.1 Metal co-catalyst. Generally, a metal co-catalyst refers to noble metals such as Au, Ag, and Pt. By depositing the noble metals on a photocatalyst, a Schottky barrier can be formed on the interface, and the metal nanoparticles can become electron traps to facilitate the separation of photogenerated charges.[77] Pt is one of the most common co-catalysts used in CO_2 reduction because of its great methane selectivity in a gas–solid system.[78] Yu *et al.* prepared g-C_3N_4 by direct calcination with thiourea as a precursor and Pt nanoparticles that were deposited for CO_2 photoreduction.[46] The deposited Pt nanoparticles absorbed nearly all the incident light, and thus increased the visible light absorption without changing the band gap of g-C_3N_4.[79] Moreover, the introduction of Pt nanoparticles promoted the generated photoelectrons to transfer from g-C_3N_4 to Pt and react with CO_2. The yield of CH_4 initially increased as the amount of deposited Pt increased from 0 to 1%, and then decreased as the loading of Pt increased to 2% or higher. Similar observations have also been reported by Chai *et al.* (Fig. 6).[47] This relative reduction in the production of CH_4 was attributed to the excess Pt that increased the negative charges on the surface of the g-C_3N_4 and promoted the recombination of electrons and holes. Another possibility is that excessive or redundant Pt covers the active sites on the surface of g-C_3N_4 and shields them from light. In another study, Du *et al.* substituted Pt nanoparticles with individual Pt atoms and found that the Pt/g-C_3N_4 catalyst preferred to reduce CO_2 to CH_4, with a rate-determining barrier of 1.16 eV and greatly enhanced visible light absorption.[48]

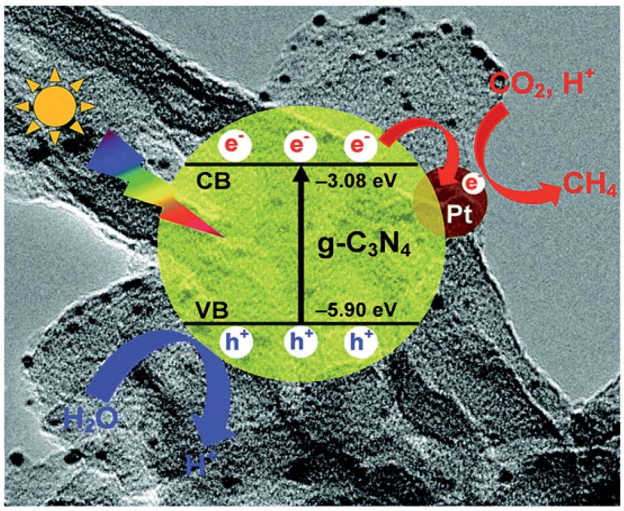

Fig. 6 Photogenerated charge transfer process in the Pt/CN system for the reduction of CO_2 to CH_4 under visible light irradiation.[47] Copyright 2014, Royal Society of Chemistry.

Other noble metals are also frequently employed to modify g-C_3N_4.[49,50] Currently, there are few CO_2 reduction systems using non-noble metals.[51,52] However, according to a DFT calculation, Mo could be an efficient co-catalyst on g-C_3N_4 for CO_2–CO conversion.[53]

3.3.2 Carbon materials. Carbon materials, *e.g.*, carbon nanodots, graphene, graphene oxide, and other similar materials, have also been employed as co-catalysts to facilitate the electron transfer on g-C_3N_4. Chai *et al.* fabricated sandwich-like graphene-g-C_3N_4 nanocomposites (GCN) by one-pot impregnation-thermal reduction.[54] The covalent bonds formed between the graphene and g-C_3N_4 endow the GCN sample with a slight redshift of the absorption band edge. The GCN sample exhibited a 2.3-fold enhancement of CH_4 yield over pure g-C_3N_4 due to the inhibited electron–hole pair recombination and increased charge transfer.

In another study, 3D porous g-C_3N_4/carbon nanosheets were prepared by simple pyrolysis and subsequent carbothermal activation.[55] Gas-phase CO_2 photoreduction experiments under simulated solar irradiation showed that the photocatalytic activity of the 3D g-C_3N_4 was 2 times that of the bulk g-C_3N_4 due to the introduction of carbon and the 3D porous structure. First, the hierarchical 3D porous architecture promoted CO_2 transportation to active sites and accelerated the diffusion of products. Second, the 3D porous structure could have increased the light-harvesting ability. Furthermore, the photogenerated electrons could have effectively drifted from g-C_3N_4 to the hybrid carbon under the action of the inner electric field due to the quantum confinement effect, which inhibited the electron–hole pairs from combining and prolonged the lifetime of the photogenerated charge carriers. Finally, according to their X-ray photoelectron spectroscopy (XPS) analysis, there were partial electron-withdrawing carbon–oxygen groups on the surface of this composite, *e.g.*, C–O, C=O, and O–C=O groups, which could have facilitated the electron flow on the external surface. Thus, the recombination of electron–hole pairs was suppressed.

Carbon quantum dots (CQDs) doped onto g-C_3N_4 can also offer many advantages in CO_2 photoreduction, such as reducing the band-gap, the electron-withdrawing effect, and the up-conversion effect.[56] Recently, Tang *et al.* reported the hole-accepting effect of carbon dots in promoting selective CO_2 reduction to methanol.[57] The microwave-synthesized carbon dots have a pure graphite structure that facilitates efficient hole transfer to carbon dots and favours electron accumulation on the surface of g-C_3N_4. Moreover, the hole-accepting carbon dots can prevent the surface adsorption of methanol, which subsequently prevents the re-oxidation of produced methanol. As a result, the carbon dot-decorated g-C_3N_4 produced methanol from water and CO_2 with nearly 100% selectivity to methanol. This work exhibited the great potential of carbon quantum dots in efficient and highly selective CO_2 photoreduction.

3.3.3 Metal oxide/sulfide/phosphide materials. Apart from carbon materials and metals, other co-catalysts are emerging, *e.g.*, metal oxide, metal sulfide, and metal phosphide. Ye *et al.* loaded chainmail Ni/NiO co-catalyst onto g-C_3N_4 to increase the photocatalytic CO_2 reduction.[58] The NiO shell over the surface of Ni particles protects Ni from being oxidized to ensure increased stability and high photoactivity of elemental Ni. Additionally, the XPS spectra of g-C_3N_4 and Ni/NiO/g-C_3N_4 indicated that g-C_3N_4 interacted with Ni/NiO *via* π–π interactions to facilitate charge carrier transfer at the interface, which can also be demonstrated by photocurrent responses, electrochemical impedance spectra, and PL spectra. The surface photovoltage (SPV) spectra and transient photovoltage (TPV) spectra of the samples indicated that the introduction of Ni/NiO endowed the catalyst with stronger generation and more efficient separation of the photogenerated charge carriers. With an adequate amount of Ni/NiO loading, the CO yield on Ni/NiO/g-C_3N_4 reached 13.95 $\mu mol\ g^{-1}\ h^{-1}$, which was approximately 9-fold higher than that on pristine g-C_3N_4.

Zhou *et al.* loaded molybdenum phosphide (MoP) onto g-C_3N_4.[59] The introduction of MoP facilitated the separation and transfer of electron hole pairs, and increased light absorption throughout the UV and visible light spectrum without changing the absorption edge of g-C_3N_4, thus endowing the photocatalyst with a 4.5-fold higher production of CO compared with pristine g-C_3N_4. Pan *et al.* prepared NiS_2 quantum dot-modified g-C_3N_4 photocatalysts by a hydrothermal method.[60] The lower Fermi level and surficial metallicity resulted in the ability of NiS_2 to become an ideal electron acceptor, which accelerated the separation of electron–hole pairs and inhibited their recombination. Additionally, the introduction of NiS_2 quantum dots provided more active sites and contributed to close interface contact. Therefore, the CO yield on NiS_2/g-C_3N_4 reached 10.68 $\mu mol\ g^{-1}\ h^{-1}$, which was 3.88 times higher than that on pristine g-C_3N_4.

Co-catalysts significantly improve the photocatalytic performance of g-C_3N_4 by facilitating the charge carrier transfer and suppressing the recombination of electron–hole pairs. It is worth noting that some metal oxides, metal phosphides, and metal sulfides can form heterojunctions together with g-C_3N_4, which is further discussed below.

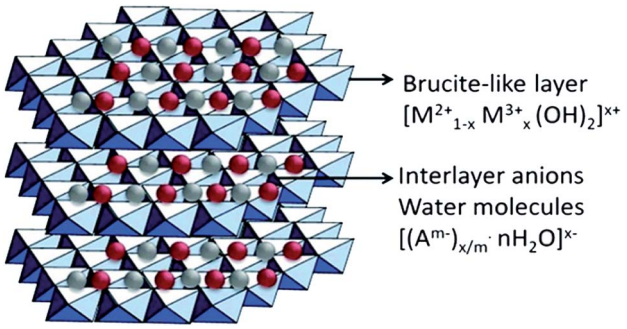

Fig. 7 Schematic illustration of layered double hydroxide structure and chemical.[80] Copyright 2017, Elsevier.

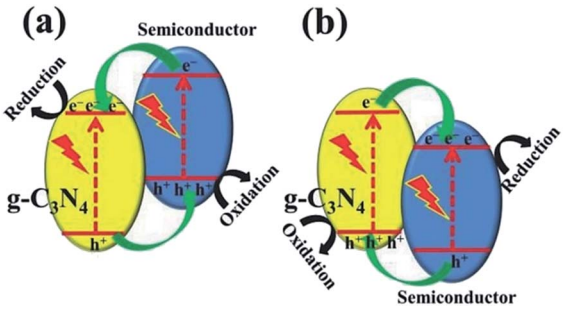

Fig. 8 Charge transfer in the conventional type II g-C_3N_4-based heterojunction systems composed of g-C_3N_4 and another semiconductor (a) with more negative CB and (b) with more positive VB.[21] Copyright 2017, Wiley-VCH.

3.4 g-C_3N_4-based composites

Combining g-C_3N_4 with other semiconductors to form heterojunctions can facilitate electron transfer, light utilization, and even CO_2 adsorption. Hence, it is a highly recommended strategy for CO_2 photocatalytic reduction using g-C_3N_4.

3.4.1 g-C_3N_4 absorbent composites. It is well known that the adsorption/activation of CO_2 is the first step in photocatalytic CO_2 reduction. However, pristine g-C_3N_4 has a limited surface area and a small number of active sites due to its stacked structure, which impedes the adsorption of g-C_3N_4. One strategy to change this is to combine g-C_3N_4 with CO_2 adsorbents.

Layered double hydroxides (LDHs) are a class of compounds made up of positively charged brucite-like layers with an interlayered region containing charge-compensating anions and solvation molecules (Fig. 7).[81] By using a general formula $[MII_{1-x}MIII_x(OH)_2]^{x+}\cdot(A^{n-})_{x/n}\cdot mH_2O$ (M = metal, A = interlayer anion), it was determined that LDHs exhibited some physicochemical properties that are in favour of CO_2 adsorption, *e.g.*, large surface areas, positive surface charges, and compositional flexibilities.[76] Xu *et al.* used Mg–Al-LDH nanosheets to enrich CO_2 on the surface of g-C_3N_4 by the exploitation of its anion-exchange capacity.[61] LDH/g-C_3N_4 was assembled *via* electrostatic interaction combined with Pd co-catalyst, and it showed a remarkably enhanced CH_4 yield compared to the yield without LDH. Moreover, enriched CO_2 existed in the form of interlayered CO_3^{2-} in the LDH, which could have been more efficiently reduced. Apart from LDH, metal organic frameworks (MOFs) have unique structural properties such as high surface area, high porosity, and low crystal density, as well as high thermal and chemical stability, and thus, they can also be utilized to enhance CO_2 adsorption on g-C_3N_4.[62]

3.4.2 g-C_3N_4-based heterojunctions. From previous studies, it is known that the most frequently used g-C_3N_4-based photocatalysts are composites of g-C_3N_4 with other semiconductors, and are called g-C_3N_4-based heterojunctions.[76]

(a) g-C_3N_4-based type II heterojunction. The heterojunction is a type of p–n junction. It refers to two semiconductor materials that have been combined through surface assembly or internal crystal interface crosslinks, which accelerates the separation of electron–hole pairs by the construction of a built-in electric field.

In terms of the energy band, heterojunctions fall into three categories: (i) type I heterojunction, where the forbidden gap of one component is completely covered by that of the other component; (ii) type II heterojunction, where the forbidden bands of the two components are staggered, and the semiconductor has a more negative CB and a less positive VB; (iii) type III heterojunction, where the forbidden bands of the two components are completely separated. The most investigated photocatalysis systems are usually type II heterojunctions. When a photocatalytic reaction takes place, the photogenerated electrons transfer from the more negative CB to the CB of the other semiconductor and generate a reduction reaction, while the holes transfer from the more positive VB to VB of the other semiconductor and generate an oxidation reaction.

One can construct a type II heterojunction system with g-C_3N_4 and another semiconductor with a more negative CB position or a more positive VB position (Fig. 8). Commonly, there are few semiconductors whose CB position is more negative than that of g-C_3N_4, and thus, it is easy to construct a g-C_3N_4-based heterojunction, as illustrated in Fig. 8b. Many metal oxides, sulfides, halides, and other semiconductors are used for such a system.[21] The construction of the heterostructure plays a significant role in its photocatalytic performance and stability.[82,83]

(b) g-C_3N_4-based Z-scheme heterojunction. The Z-scheme heterojunction, mimicking the photosynthesis of plants, was first proposed to solve the problem that a single photocatalyst could not split water to simultaneously produce both hydrogen and oxygen. A classic Z-scheme photocatalytic system consists of two photoluminescence processes and a series of redox reactions, and the electron transfer takes place in two optical systems (SI and SII).[84] Different from type II heterojunctions, the electrons excited on SI transfer to SII through an electronic mediator and combine with holes generated on SII (Fig. 9a). Consequently, the electron–hole pairs generated in each semiconductor are separated, while the high reduction and oxidation abilities of the electrons and holes, respectively, are maintained.[21,85] This mechanism involved with a mediator is known as the indirect Z-scheme. There is another type of mediator-free charge transfer mechanism, namely, the direct Z-scheme mechanism. In the direct Z-scheme mechanism, the photogenerated electrons on

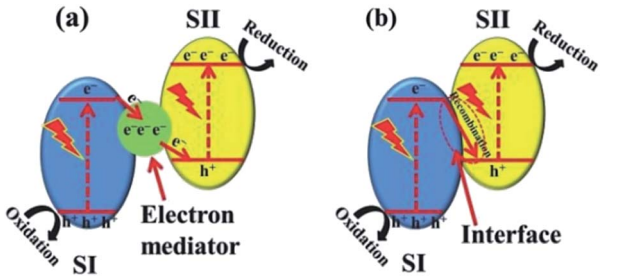

Fig. 9 Z-scheme charge transfer between semiconductors (a) with or (b) without an electron mediator.[21] Copyright 2017, Wiley-VCH.

SI are directly transferred to SII and combined with the holes in SII (Fig. 9b).[86,87] This results in direct contact between the two semiconductors and accelerates the charge transfer between the two components, which not only increases the reaction efficiency but also reduces the cost.

Li *et al.* synthesized an indirect Z-scheme BiOI/g-C_3N_4 heterojunction using a simple deposition method.[63] The composite at an optimal fraction of 7.4 wt% BiOI exhibited a significantly enhanced CO yield of 17.9 μmol g^{-1} in a CO_2 photoreduction test. The indirect Z-scheme charge transfer mechanism was confirmed through a series of characterizations including UPS, XPS, and DRS. A contrast test was executed to confirm the roles of intermediate I_3^-/I^- pairs. In another study, an Al–O-bridged g-C_3N_4/α-Fe_2O_3 heterojunction was prepared using a two-step wet chemical method with $AlCl_3$ aqueous solution as the Al–O source.[64] The Al–O bridges significantly promoted charge transfer and separation and consequently enhanced the CO_2 photoreduction performance (Fig. 10). The composite exhibited an approximately 4-fold enhancement of CO production (24 μmol g^{-1} h^{-1}). Due to the existence of a charge transfer mediator, this type of Z-scheme heterojunction requires well-designed structures to achieve high charge separation and transfer efficiencies. In contrast, the charge transfers in direct Z-scheme heterojunctions are accelerated by the interface contacts, and there are high reaction efficiencies and low cost with direct Z-scheme heterojunctions. Therefore, there has been increasing interest in direct Z-scheme heterojunctions in recent years.

Wong *et al.* also fabricated a direct Z-scheme heterojunction consisting of urchin-shaped α-Fe_2O_3 and a g-C_3N_4 nanosheet.[65] Without using any sacrificial agent or co-catalyst, the Z-scheme hybrid had a 2.2-fold higher CO evolution rate as compared to pristine g-C_3N_4, consisting of up to 27.2 μmol g^{-1} h^{-1}, which is also higher than that of an Al–O-bridged g-C_3N_4/α-Fe_2O_3 heterojunction. The introduction of 3D α-Fe_2O_3 not only narrows the band gap, increases the light absorption, and results in a high usage of optical energy, but it also increases the binding energy and CO_2 adsorption so that additional CO_2 molecules can participate in the reaction over a longer time span. Additionally, the direct Z-scheme structure facilitates the electron–hole separation in both α-Fe_2O_3 and g-C_3N_4, thus improving the reduction ability of photoelectrons in the conduction band of g-C_3N_4. The improved light harvesting, CO_2 adsorption, and

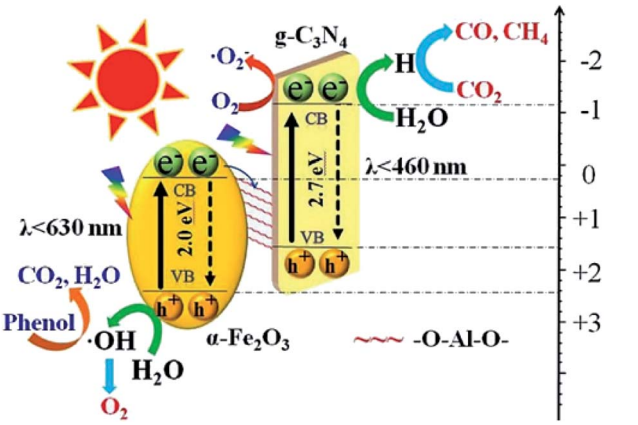

Fig. 10 Schematic showing the transfer and separation of photo-induced charges in the fabricated Al–O-bridged g-C_3N_4/α-Fe_2O_3 nanocomposites and the induced photochemical reactions.[64] Copyright 2018, Elsevier.

separation of charge carriers all contributed to the improved CO_2 photoreduction performance.

There are many other materials that can be compounded with g-C_3N_4 to fabricate direct Z-scheme heterojunctions for photocatalytic CO_2 reductions, *e.g.*, ZnO, NiAl-LDH, and Bi_2S_3. Most of these are also well designed in terms of structure for further enhancements in CO_2 photoreduction yields.[66–68] For instance, Ogale *et al.* synthesized a 2D g-C_3N_4/NiAl-LDH heterojunction with strong electrostatic interactions between positively charged NiAl-LDH and negatively charged g-C_3N_4.[66] The enhancement of the photocatalytic activity was mainly ascribed to the excellent interfacial contacts at the 2D/2D interface. The large contact area between the NiAl-LDH and g-C_3N_4 subsequently suppressed charge carrier recombination and improved the transfer and separation of photogenerated charge carriers. Guo *et al.* synthesized Bi_2S_3 quantum dots/g-C_3N_4 composites, where the Bi_2S_3 quantum dots were uniformly dispersed on g-C_3N_4, and this increased the light absorption and the separation of electron–hole pairs. A series of characterizations demonstrated the Z-scheme mechanism. The heterojunction exhibited 4-fold higher CO yield than the pristine g-C_3N_4.[67]

The photocatalytic mechanism of Z-scheme heterojunctions can be revealed by PL analysis and DFT calculations. Yu *et al.* prepared a g-C_3N_4/ZnO binary composite for photocatalytic CO_2 reduction to CH_3OH.[68] The photocatalytic activity exhibited 2.3-fold enhancement compared with pure g-C_3N_4. The possible photocatalytic mechanism was verified by carrying out a PL analysis of hydroxyl radicals (•OH) produced on pure g-C_3N_4, pure ZnO, and the composite. In terms of thermodynamics, the •OH and $•O_2^-$ can only be produced by photogenerated holes from the VB of the ZnO and electrons from the CB of the g-C_3N_4, respectively. According to the double-transfer mechanism, neither •OH nor $•O_2^-$ could be produced in the composite system, which implied that it was likely that the charge transfer followed the Z-scheme mechanism. This observation was supported by calculating the charge carrier effective mass and separating tendency of photogenerated electron–hole pairs

using a DFT calculation. It was found that ZnO has a much higher relative effective mass of electrons and holes ($D = m_h^*/m_e^*$), indicating that the excited electrons of ZnO have a higher tendency to transfer, and thus, the charge transfer is more likely to originate from the ZnO to g-C_3N_4 instead of the opposite direction.[88] These findings support the rationality of the Z-scheme mechanism.

3.4.3 Photocatalyst based on g-C_3N_4 and metal complexes. As mentioned before, compared to traditional semiconductor catalysts, metal complexes possess higher efficiency and selectivity, but poor oxidation ability and recycling ability, which limit their utilization.[89,90] Therefore, g-C_3N_4 and metal complexes are combined in some studies, where the metal complex and g-C_3N_4 act as active sites and light-harvesting units, respectively, to combine their advantages.

Maeda *et al.* synthesized a heterogeneous photocatalyst consisting of a ruthenium (Ru) complex and g-C_3N_4. The former served as the catalytic unit and the latter as a light-harvesting unit, respectively. The electronic interactions between the two components enable the electrons to transfer from g-C_3N_4 into ruthenium.[69] With *trans*-(Cl)-[Ru[4,4′-$(CH_2PO_3H_2)_2$-2,2′-bipyridine]$(CO)_2Cl_2$] (RuP) as catalyst and a DMA : TEOA mixture (4 : 1, v/v) as solvent, CO_2 was reduced to HCOOH and CO with a selectivity of 80% for HCOOH, and the turnover number (TON) reached 1061 after 20 h of irradiation. The apparent quantum yield was 5.7% at 400 nm, which is higher than the performance reported in earlier studies. Jain *et al.* combined g-C_3N_4 with cobalt(II) phthalocyanine tetracarboxylate (CoPc-COOH) in various ratios to form numerous complex-semiconductor hybrid photocatalysts.[70] The CO_2 photoreduction activities of the synthesized CoPc-COOH, g-C_3N_4, and g-C_3N_4/CoPc-COOH were tested in a water/DMF environment using triethylamine (TEA) as a sacrificial agent. After a 24 h period of visible light irradiation, the CH_4 yield of the g-C_3N_4/CoPc-COOH was 12.9 mmol g^{-1}, which is 7.3 and 10.9 times higher than that of CoPc-COOH and g-C_3N_4, respectively. The improved photocatalytic efficiency was ascribed to the higher CO_2 concentration resulting from the binding ability of CoPc-COOH to CO_2.

For the g-C_3N_4/metal complex photocatalytic system, the interaction between g-C_3N_4 and metal complex plays an important role in the enhancement of charge transfer migration and suppression of charge recombination. To maximize the interaction, either π–π interaction between the tri-*s*-triazine unit of g-C_3N_4 and organic ligands or hydrogen bonds/covalent bonds between the functional groups can make positive contributions.

4. Conclusions

We reviewed the recent progress on g-C_3N_4-based materials for photocatalytic reduction of CO_2. Furthermore, the basic properties of g-C_3N_4, and the principles and main steps of CO_2 photoreduction have been critically elaborated. Additionally, different types of g-C_3N_4-based composites were compared, *e.g.*, pristine g-C_3N_4, non-metal doped g-C_3N_4, g-C_3N_4 with co-catalysts, g-C_3N_4-based semiconductors, and g-C_3N_4/metal complex. Among the g-C_3N_4-based photocatalysts for CO_2 reduction, g-C_3N_4-based semiconductors are most frequently used and have attracted the most interest. The Z-scheme structure, especially direct Z-scheme heterojunctions, realize charge transfer through interface contact, which accelerates charge transfer and leads to increased reaction efficiency and reduced cost. Hence, direct Z-scheme heterojunctions have attract more interest in recent years. Moreover, combined with other treatments such as elemental doping and structural fabrication, the photocatalytic efficiency of g-C_3N_4-based materials can be further increased. However, compared to g-C_3N_4/metal complex systems, a heterogeneous photocatalysis system based on semiconductor photocatalysts exhibits relatively lower utilization of light and depressed photocatalytic efficiency. By improving the interaction between the active sites and light-harvesting unit and optimizing the reaction conditions, g-C_3N_4/metal complex photocatalysts can increase the conversion efficiency greater than 10 fold, but this can complicate separation and recycling.

In view of the above challenges, significant efforts have been made to combine homogeneous and heterogeneous photocatalysts to obtain high efficiency and high oxidation ability. For the heterogeneous photocatalytic system, strategies were mainly focused on three approaches: (i) tuning the surface properties of g-C_3N_4 to enhance the adsorption or activation of CO_2, (ii) tuning the band structure for more optimal light utilization and photogenerated charge transfer, and (iii) reasonable design of a reaction pathway to accelerate the interface reaction. With laboratory-grade reactions, greater than 90% yield and selectivity of a product could be attained, which is much better than an industrial grade CO_2 conversion. Due to financial constraints and industrial scale, these systems are not widely applicable to industrial production. However, future recommended pathways will enable the development of more efficient and sustainable technologies for the g-C_3N_4 photoreduction of CO_2 so that a cleaner environment will exist for future generations.

Conflicts of interest

There are no conflicts to declare.

Acknowledgements

This work was supported by National Key R&D Program of China [2016YFA0202900, 2016YFC1402400], National Natural Science Foundation of China [51672173, U1733130], MOE Joint Foundation [6141A02022264], Shanghai Science and Technology committee [17JC1400700, 18520744700, 18JC1410500], Science and Technology Planning Project of Guangdong Province [2016A010103018]. The authors gratefully acknowledge the Shanghai Synchrotron Radiation Facility (SSRF).

References

1 M. Aresta, A. Dibenedetto and A. Angelini, *Chem. Rev.*, 2014, **114**, 1709–1742.

2 X. Liu, S. Inagaki and J. Gong, *Angew. Chem., Int. Ed.*, 2016, **55**, 14924–14950.
3 T. Inoue, A. Fujishima, S. Konishi and K. Honda, *Nature*, 1979, **277**, 637–638.
4 J. Hawecker, J. M. Lehn and R. Ziessel, *J. Chem. Soc., Chem. Commun.*, 1983, **9**, 536–538.
5 I. Willner, D. Mandler and A. Riklin, *J. Chem. Soc., Chem. Commun.*, 1986, **13**, 1022–1024.
6 W. Wang, J. Soulis, Y. J. Yang and P. Biswas, *Aerosol Air Qual. Res.*, 2014, **14**, 533–549.
7 J. Qin, V. A. Larionov, K. Harms and E. Meggers, *ChemSusChem*, 2019, **12**, 320–325.
8 Y. Guo, P. Yang, S. Zhang, B. Jiang, A. Khan, L. Zhu, Z. Fu and Z. Fan, *Iran. Polym. J.*, 2018, **27**, 153–159.
9 F. Chen, X. Jiang, L. Zhang, R. Lang and B. Qiao, *Chin. J. Catal.*, 2018, **39**, 893–898.
10 W. Zhou, W. Li, J. Wang, Y. Qu, Y. Yang, Y. Xie, K. Zhang, L. Wang, H. Fu and D. Zhao, *J. Am. Chem. Soc.*, 2014, **136**, 9280–9283.
11 N. Tian, Y. Zhang, X. Li, K. Xiao, X. Du, F. Dong, G. I. N. Waterhouse, T. Zhang and H. Huang, *Nano Energy*, 2017, **38**, 72–81.
12 C. Li, G. Chen, J. Sun, J. Rao, Z. Han, Y. Hu, W. Xing and C. Zhang, *Appl. Catal., B*, 2016, **188**, 39–47.
13 Q. Zhang, D. Q. Lima, I. Lee, F. Zaera, M. Chi and Y. Yin, *Angew. Chem., Int. Ed.*, 2011, **50**, 7088–7092.
14 L. Jiang, X. Yuan, G. Zeng, X. Chen, Z. Wu, J. Liang, J. Zhang, H. Wang and H. Wang, *ACS Sustainable Chem. Eng.*, 2017, **5**, 5831–5841.
15 T. Xu, L. Zhang, H. Cheng and Y. Zhu, *Appl. Catal., B*, 2011, **101**, 382–387.
16 S. D. Perera, R. G. Mariano, K. Vu, N. Nour, O. Seitz, Y. Chabal and K. J. Balkus, *ACS Catal.*, 2012, **2**, 949–956.
17 C. Chen, W. Cai, M. Long, B. Zhou, Y. Wu, D. Wu and Y. Feng, *ACS Nano*, 2010, **4**, 6425–6432.
18 Y. Wang, X. Wang and M. Antonietti, *Angew. Chem., Int. Ed.*, 2012, **51**, 68–89.
19 E. G. Gillan, *Chem. Mater.*, 2000, **12**, 3906–3912.
20 J. Zhang, B. Wang and X. Wang, *Acta Phys.-Chim. Sin.*, 2013, **29**, 1865–1876.
21 J. Fu, J. Yu, C. Jiang and B. Cheng, *Adv. Energy Mater.*, 2018, **8**, 1701503.
22 L. Jiang, X. Yuan, Y. Pan, J. Liang, G. Zeng, Z. Wu and H. Wang, *Appl. Catal., B*, 2017, **217**, 388–406.
23 X. Wang, K. Maeda, A. Thomas, K. Takanabe, G. Xin, J. M. Carlsson, K. Domen and M. Antonietti, *Nat. Mater.*, 2009, **8**, 76–80.
24 J. Mao, T. Peng, X. Zhang, K. Li, L. Ye and L. Zan, *Catal. Sci. Technol.*, 2013, **3**, 1253–1260.
25 Y. Li, R. Ma, L. He and Z. Diao, *Catal. Sci. Technol.*, 2014, **4**, 1498–1512.
26 F. D. Meylan, V. Moreau and S. Erkman, *J. CO_2 Util.*, 2015, **12**, 101–108.
27 J. Wu, Y. Huang, W. Ye and Y. Li, *Adv. Sci.*, 2017, **4**, 1700194.
28 J. Lee, D. C. Sorescu and X. Deng, *J. Am. Chem. Soc.*, 2011, **133**, 10066–10069.
29 Q. Lu, Y. Yu, Q. Ma, B. Chen and H. Zhang, *Adv. Mater.*, 2016, **28**, 1917–1933.
30 Y. S. Seo and S. G. Oh, *Korean J. Chem. Eng.*, 2019, **36**, 2118–2124.
31 G. Dong and L. Zhang, *J. Mater. Chem.*, 2012, **22**, 1160–1166.
32 Y. Zheng, L. Lin, X. Ye, F. Guo and X. Wang, *Angew. Chem., Int. Ed.*, 2014, **53**, 11926–11930.
33 P. Xia, B. Zhu, J. Yu, S. Cao and M. Jaroniec, *J. Mater. Chem. A*, 2017, **5**, 3230.
34 M. Shen, L. Zhang, M. Wang, J. Tian, X. Jin, L. Guo, L. Wang and J. Shi, *J. Mater. Chem. A*, 2019, **7**, 1556–1563.
35 J. Tang, X. Kong, B. J. Ng, Y. H. Chew, A. R. Mohamed and S. P. Chai, *Catal. Sci. Technol.*, 2019, **9**, 2335–2343.
36 X. Wu, H. Ma, W. Zhong, J. Fan and H. Yu, *Appl. Catal., B*, 2020, **271**, 118899.
37 X. Wu, D. Gao, H. Yu and J. Yu, *Nanoscale*, 2019, **11**, 9608.
38 J. Fu, K. Liu, K. Jiang, H. Li, P. An, W. Li, N. Zhang, H. Li, X. Xu, H. Zhou, D. Tang, X. Wang, X. Qiu and M. Liu, *Adv. Sci.*, 2019, **6**, 1900796.
39 B. Liu, L. Ye, R. Wang, J. Yang, Y. Zhang, R. Guan, L. Tian and X. Chen, *ACS Appl. Mater. Interfaces*, 2018, **10**, 4001–4009.
40 K. Wang, Q. Li, B. Liu, B. Cheng, W. Ho and J. Yu, *Appl. Catal., B*, 2015, **176–177**, 44–52.
41 S. Samanta, R. Yadav, A. Kumar and A. K. Sinha, *Appl. Catal., B*, 2019, **259**, 118054.
42 K. Wang, J. Fu and Y. Zheng, *Appl. Catal., B*, 2019, **254**, 270–282.
43 S. Wang, J. Zhan, K. Chen, A. Ali, L. Zeng, H. Zhao, W. Hu, L. Zhu and X. Xu, *ACS Sustainable Chem. Eng.*, 2020, **8**, 8214–8222.
44 H. Zhang, Y. Tang, Z. Liu, Z. Zhu, X. Tang and Y. Wang, *Chem. Phys. Lett.*, 2020, **751**, 137467.
45 Z. Zhu, X. Tang, W. Fan, Z. Liu, P. Huo, T. Wang, Y. Yan and C. Li, *J. Alloys Compd.*, 2019, **775**, 248–258.
46 J. Yu, K. Wang, W. Xiao and B. Cheng, *Phys. Chem. Chem. Phys.*, 2014, **16**, 11492–11501.
47 W. J. Ong, L. L. Tan, S. P. Chai and S. T. Yong, *Dalton Trans.*, 2015, **44**, 1249–1257.
48 G. Gao, Y. Jiao, E. R. Waclawik and A. Du, *J. Am. Chem. Soc.*, 2016, **138**, 6292–6297.
49 X. Lan, Y. Li, C. Du, T. She, Q. Li and G. Bai, *Chem.–Eur. J.*, 2019, **25**, 8560–8569.
50 H. Li, Y. Gao, Z. Xiong, C. Liao and K. Shih, *Appl. Surf. Sci.*, 2018, **439**, 552–559.
51 F. Gonell, A. V. Puge, B. Julian-Lopez, H. Garcia and A. Corma, *Appl. Catal., B*, 2016, **180**, 263–270.
52 S. Neatu, J. A. Macia-Agullo, C. Patricia and H. Garcia, *J. Am. Chem. Soc.*, 2014, **136**, 15969–15976.
53 P. Li, F. Wang, S. Wei, X. Li and Y. Zhou, *Phys. Chem. Chem. Phys.*, 2017, **19**, 4405–4410.
54 W. J. Ong, L. L. Tan, S. P. Chai and S. Yong, *Chem. Commun.*, 2015, **51**, 858–861.
55 Y. Wang, Q. Xia, X. Bai, Z. Ge, Q. Yang, C. Yin, S. Kang, M. Dong and X. Li, *Appl. Catal., B*, 2018, **239**, 196–203.
56 H. Feng, Q. Guo, Y. Xu, T. Chen, Y. Zhou, Y. Wang, M. Wang and D. Shen, *ChemSusChem*, 2018, **11**, 4256–4261.

57 Y. Wang, X. Liu, X. Han, R. Godin, J. Chen, W. Zhou, C. Jiang, J. F. Thompson, K. B. Mustafa, S. A. Shevlin, J. R. Durrant, Z. Guo and J. Tang, *Nat. Commun.*, 2020, **11**, 2531.
58 C. Han, R. Zhang, Y. Ye, L. Wang, Z. Ma, F. Su, H. Xie, Y. Zhou, P. K. Wong and L. Ye, *J. Mater. Chem. A*, 2019, **7**, 9726.
59 J. Tang, D. Yang, W. Zhou, R. Guo, W. Pan and C. Huang, *J. Catal.*, 2019, **370**, 79–87.
60 H. Qin, R. Guo, X. Liu, X. Shi, Z. Wang, J. Tang and W. Pan, *Colloids Surf., A*, 2020, **600**, 124912.
61 J. Hong, W. Zhang, Y. Wang, T. Zhou and R. Xu, *ChemCatChem*, 2014, **6**, 2315–2321.
62 Y. S. Bae and R. Q. Snurr, *Angew. Chem., Int. Ed.*, 2011, **50**, 11586–11596.
63 J. Wang, H. Yao, Z. Fan, L. Zhang, J. Wang, S. Zang and Z. Li, *ACS Appl. Mater. Interfaces*, 2016, **8**, 3765–3775.
64 J. Wang, C. Qin, H. Wang, M. Chu, A. Zada, X. Zhang, J. Li, F. Raziq, Y. Qu and L. Jing, *Appl. Catal., B*, 2018, **221**, 459–466.
65 Z. Jiang, W. Wan, H. Li, S. Yuan, H. Zhao and P. Wong, *Adv. Mater.*, 2018, **30**, 1706108.
66 S. Tonda, S. Kumar, M. Bhardwaj, P. Yadav and S. Ogale, *ACS Appl. Mater. Interfaces*, 2018, **10**, 2667–2678.
67 R. Guo, X. Liu, H. Qin, Z. Wang, X. Shi, W. Pan, Z. Fu, J. Tang, P. Jia, Y. Miao and J. Gu, *Appl. Surf. Sci.*, 2020, **500**, 144059.
68 W. Yu, D. Xu and T. Peng, *J. Mater. Chem. A*, 2015, **3**, 19936–19947.
69 R. Kuriki, K. Sekizawa, O. Ishitani and K. Maeda, *Angew. Chem., Int. Ed.*, 2015, **127**, 2436–2439.
70 A. Kumar, P. Prajapati, K. Pankaj, M. S. Aathira, A. Bansiwal, R. Boukherroub and S. L. Jain, *J. Colloid Interface Sci.*, 2019, **543**, 201–213.
71 G. Zhang, M. Zhang, X. Ye, X. Qiu, S. Lin and X. Wang, *Adv. Mater.*, 2014, **26**, 805–809.
72 G. Zhang, G. Li, T. Heil, S. Zafeiratos, F. Lai, A. Savateev, M. Antonietti and X. Wang, *Angew. Chem., Int. Ed.*, 2019, **58**, 3433–3437.
73 D. Masih, Y. Ma and S. Rohani, *Appl. Catal., B*, 2017, **206**, 556–588.
74 S. Cao, H. Li, T. Tong, H. Chen, A. Yu, J. Yu and H. Chen, *Adv. Funct. Mater.*, 2018, **28**, 1802169.
75 N. Sagara, S. Kamimura, T. Tsubota and T. Ohno, *Appl. Catal., B*, 2016, **192**, 193–198.
76 Z. Sun, H. Wang, Z. Wu and L. Wang, *Catal. Today*, 2018, **300**, 160–172.
77 J. Hong, W. Zhang, Y. Wang, T. Zhou and R. Xu, *ChemCatChem*, 2014, **6**, 2315–2321.
78 Q. Zhai, S. Xie, W. Fan, Q. Zhang, Y. Wang, W. Deng and Y. Wang, *Angew. Chem., Int. Ed.*, 2013, **52**, 5776–5779.
79 Q. Gu, J. Long, H. Zhuang, C. Zhang, Y. Zhou and X. Wang, *Phys. Chem. Chem. Phys.*, 2014, **16**, 12521–12534.
80 M. Zubair, M. Daud, G. McKay, F. Shehzad and M. A. Al-Harthi, *Appl. Clay Sci.*, 2017, **143**, 279–292.
81 Q. Wang and D. O'Hare, *Chem. Rev.*, 2012, **112**, 4124–4155.
82 H. Wang, L. Zhang, Z. Chen, J. Hu, S. Li, Z. Wang, J. Liu and X. Wang, *Chem. Soc. Rev.*, 2014, **43**, 5234–5244.
83 H. Li, Y. Zhou, W. Tu, J. Ye and Z. Zou, *Adv. Funct. Mater.*, 2015, **25**, 998–1013.
84 K. Maeda, *ACS Catal.*, 2013, **3**, 1486–1503.
85 H. Tada, T. Mitsui, T. Kiyonaga, T. Akita and K. Tanaka, *Nat. Mater.*, 2006, **5**, 782–786.
86 J. Low, C. Jiang, B. Cheng, S. Wageh, A. A. Al-Ghamdi and J. Yu, *Small Methods*, 2017, **1**, 1700080.
87 P. Zhou, J. Yu and M. Jaroniec, *Adv. Mater.*, 2014, **26**, 4920–4935.
88 H. Zhang, L. Liu and Z. Zhou, *Phys. Chem. Chem. Phys.*, 2011, **14**, 1286–1292.
89 B. Kumar, M. Llorente, J. Froehlich, T. Dang, A. Sathrum and C. P. Kubiak, *Annu. Rev. Phys. Chem.*, 2012, **63**, 541–569.
90 T. Yui, Y. Tamaki, K. Sekizawa and O. Ishitani, *Top. Curr. Chem.*, 2011, **303**, 151–184.

